PAPER • OPEN ACCESS

Plasma beta dependence of turbulent transport suggesting an advantage of weak magnetic shear from local and global gyrokinetic simulations

To cite this article: A. Ishizawa *et al* 2024 *Nucl. Fusion* **64** 066008

OPEN ACCESS
IOP Publishing | International Atomic Energy Agency
Nuclear Fusion
Nucl. Fusion **64** (2024) 066008 (11pp)
https://doi.org/10.1088/1741-4326/ad3d6d

Plasma beta dependence of turbulent transport suggesting an advantage of weak magnetic shear from local and global gyrokinetic simulations

A. Ishizawa*, Y. Kishimoto, K. Imadera, Y. Nakamura and S. Maeyama[1]

Graduate School of Energy Science, Kyoto University, Uji 611-0011, Japan
[1] National Institute for Fusion Science, Toki 509-5292, Japan

E-mail: ishizawa@energy.kyoto-u.ac.jp

Received 14 January 2024, revised 20 March 2024
Accepted for publication 11 April 2024
Published 23 April 2024

Abstract

A higher plasma β is desirable for realizing high performance fusion reactor, in fact, one of the three goals of JT-60SA project is to achieve a high-β regime. We investigate key physical processes that regulate the β dependence of turbulent transport in L-mode plasmas by means of both local and global gyrokinetic simulations. From local simulations, we found that the turbulent transport does not decrease as β increases, because the electromagnetic stabilizing effect is canceled out by the increase of the Shafranov shift. This influence of the Shafranov shift is suppressed when the magnetic shear is weak, and thus the electromagnetic stabilization is prominent in weak shear plasmas, suggesting an advantage of weak magnetic shear plasmas for achieving a high-β regime. In high β regime, local gyrokinetic simulations are suffered from the non-saturation of turbulence level. In global simulations, by contrast, the electromagnetic turbulence gets saturated by the entropy advection in the radial direction to avoid the zonal flow erosion due to magnetic fluctuations. This breakthrough enables us to explore turbulent transport at a higher β regime by gyrokinetic simulations.

Keywords: plasma turbulence, magnetic confinement fusion, nonlinear phenomena in plasmas, plasma fusion

(Some figures may appear in colour only in the online journal)

1. Introduction

Understanding the β dependence of plasma confinement is important for predicting the fusion reaction rate that is proportional to the pressure, and the bootstrap current production for realizing steady-state operation of tokamaks, where $\beta = 8\pi p/B^2$ is the thermal pressure normalized by magnetic pressure. Experimental studies show no clear trends of β dependencies of plasma confinement, and their tendencies of β-scaling of confinement time are contradictory [1–5]. One of the main causes of confinement degradation is drift-wave induced transport in the core region, and thus understanding the β dependence of turbulent transport at the core is crucial for predicting the β dependence of the confinement.

Turbulent fluctuations are electromagnetic in finite β plasmas, and magnetic fluctuations are known to reduce the linear growth rate of ion temperature gradient (ITG) modes

* Author to whom any correspondence should be addressed.

[6–8], suggesting reduction of turbulence level with increasing β [9–13]. The electromagnetic stabilization is demonstrated in the analysis of JET and ASDEX Upgrade plasmas [5, 14–21]. However, finite β effects are not only magnetic fluctuations but also an equilibrium magnetic field change such as the Shafranov shift. Recent study shows that the electromagnetic stabilization on the ITG mode is canceled out by the Shafranov shift effect, as a result, the turbulent transport does not decrease with increasing β in several β scans [22, 23]. Here, the Shafranov shift is the shift of the magnetic axis to the outer-board of the torus and is proportional to the β value. It is also found that the influence of the Shafranov shift becomes small for the weak magnetic shear $s=(r/q)dq/dr$ plasmas. These results are obtained not only from the s-α model [22] but also from numerically calculated MHD equilibrium states for each value of β [23]. It is remarked that the s-α model is a widely used analytical equilibrium magnetic field configuration [24–27], though advanced analytical models have been developed [28, 29]. The absence of the electromagnetic stabilization is also shown in β scans of ITG modes in Wendelstein 7-X plasmas when MHD equilibrium states are calculated for each value of β [30], while the mechanism may be different from that presented in this paper, because the global magnetic shear of W7-X is small, suggesting the global magnetic shear might not be a reliable explanation on the β dependence for complicated geometries.

Magnetic fluctuations also play an important role in zonal flow production through the Maxwell stress. The fluctuations causes stochastic magnetic field and suppress zonal-flow shear [31–33], resulting in an enhancement of turbulence level with increasing β. Local gyrokinetic simulations show that this process causes the non-saturation of ITG turbulence above a critical β value equal to a fraction of the kinetic ballooning mode (KBM) stability limit [34–36]. The global effect is found to be a key to resolve the problem, and leads to a quasi-steady turbulent state [37–42]. In addition, global simulations enable us to evaluate turbulent transport in zero magnetic shear region which can appear in plasmas with weak or reversed magnetic shear [43, 44], from which internal transport barrier is initiated in higher input power regime [45].

In this paper, we newly carry out nonlinear simulations and report the β dependence of turbulent transport evaluated by nonlinear simulations for other plasma parameters including JET plasmas than the CBC DIII-D parameter that is studied in our previous work [22, 23] by means of local gyrokinetic simulations. Our new results show an increase of turbulent transport with increasing β. The results also elucidate the magnetic shear dependence of the non-decrease of turbulent transport and imply that the influence of the Shafranov shift is suppressed in weak magnetic shear plasmas. It is also presented that the turbulent transport by the trapped electron modes (TEM) increases with β.

It is also found that global simulations are useful for studying turbulent transport at high-β regime because these simulations are not suffered from the non-saturation trouble in turbulence simulations. This is due to the global entropy advection in the radial direction to avoid the zonal flow erosion due to magnetic fluctuations [41]. As a result, we can study turbulence at a higher β than the corresponding local simulation. In this paper, we newly present turbulent transport evaluated from nonlinear simulations of the ITG turbulence at finite β.

The organization of the remainder of this paper is as follows. Section 2 describes the β dependence of turbulent transport focusing on the influence of magnetic shear by local gyrokinetic simulations with/without the Shafranov shift effects. Section 3 presents the β dependence of turbulent transport by global gyrokinetic simulations. We conclude with a summary of our results in section 4.

2. β dependence of turbulent transport by local simulations

We present our results from the local gyrokinetic simulation code GKV [12, 46] by using the s-α model which is a simple model including the magnetic field change such as the Shafranov shift due to finite β. GKV is a local simulation code solving the gyrokinetic equation for the perturbed distribution function $\delta f(x,y,z,v_\parallel,\mu,t)$ with the gyrokinetic Poisson equation and Ampere's law using the flux tube coordinate, $x=\frac{q(\psi_0)}{B_0 r(\psi_0)}(\psi-\psi_0)$, $y=\frac{-r(\psi_0)}{q(\psi_0)}(\alpha-\alpha_0)$, and $z=\theta$, where $\alpha=\zeta-q(\psi)\theta$ is the magnetic field line label, ψ is the magnetic flux, θ is the poloidal angle, and the tube is located on a field line with $\psi=\psi_0$ and $\alpha=\alpha_0$ [47]. In the s-α model, the square of the perpendicular wavenumber is $k_\perp^2=k_y^2[1+(s(z-\theta_k)-\alpha\sin z)^2]$, and the magnetic drift is $\omega_{\rm ds}=\frac{-k_y}{q_s R_0 B}(m_s v_\parallel^2+\mu B)[\cos z+(s(z-\theta_k)-\alpha\sin z)\sin z]$, where $\theta_k=-k_x/(sk_y)$ and $\alpha=-q_0^2R_0\beta\frac{1}{p}\frac{dp}{dr}$ is the pressure modulation parameter.

2.1. Linear growth rate

We compare two β scans with and without the Shafranov shift, which are referred as with-Shafranov-shift and wo-Shafranov-shift respectively, for AUG shot No. 29224 ($\rho=0.5$, $q=1.34$, $s=1.08$, $R_0/L_n=0.263$, $R_0/L_{Ti}=R_0/L_{Te}=5.9175$, $T_e/T_i=1$), and JET shot No. 66404 ($\rho=0.33$, $q=1.8$, $s=0.7$, $R_0/L_n=3.8$, $R_0/L_{Ti}=8.6$, $R_0/L_{Te}=5.5$, $T_e/T_i=0.88$), and JET shot No. 75225 ($\rho=0.33$, $q=1.1$, $s=0.16$, $R_0/L_n=2.4$, $R_0/L_{Ti}=6.2$, $R_0/L_{Te}=3.4$, $T_e/T_i=0.83$ and $\rho=0.64$, $q=1.74$, $s=1.44$, $R_0/L_n=2.44$, $R_0/L_{Ti}=4.08$, $R_0/L_{Te}=5.8$, $T_e/T_i=0.93$) parameters in references [14–19], where ρ is the normalized radial location and s is the global magnetic shear at the radius. In our wo-Shafranov-shift scan, we set $\alpha=0$ in the s-α model.

Figure 1 presents the linear growth rate as a function of β_i with (with-Shafranov-shift) and without (wo-Shafranov-shift) the Shafranov shift. In the AUG shot No. 29224 ($s=1.08$), JET shot No. 66404 ($s=0.7$) and JET shot No. 75225 ($s=0.16$ at $\rho=0.33$) cases, we observe the electromagnetic stabilization of the ITG mode with increasing β for the wo-Shafranov-shift scan. On the other hand, the linear growth rates in the with-Shafranov-shift scans are enhanced from the corresponding wo-Shafranov-shift scans, and thus the electromagnetic stabilizing effect is suppressed by the Shafranov shift. The influence of the Shafranov shift is strong for the

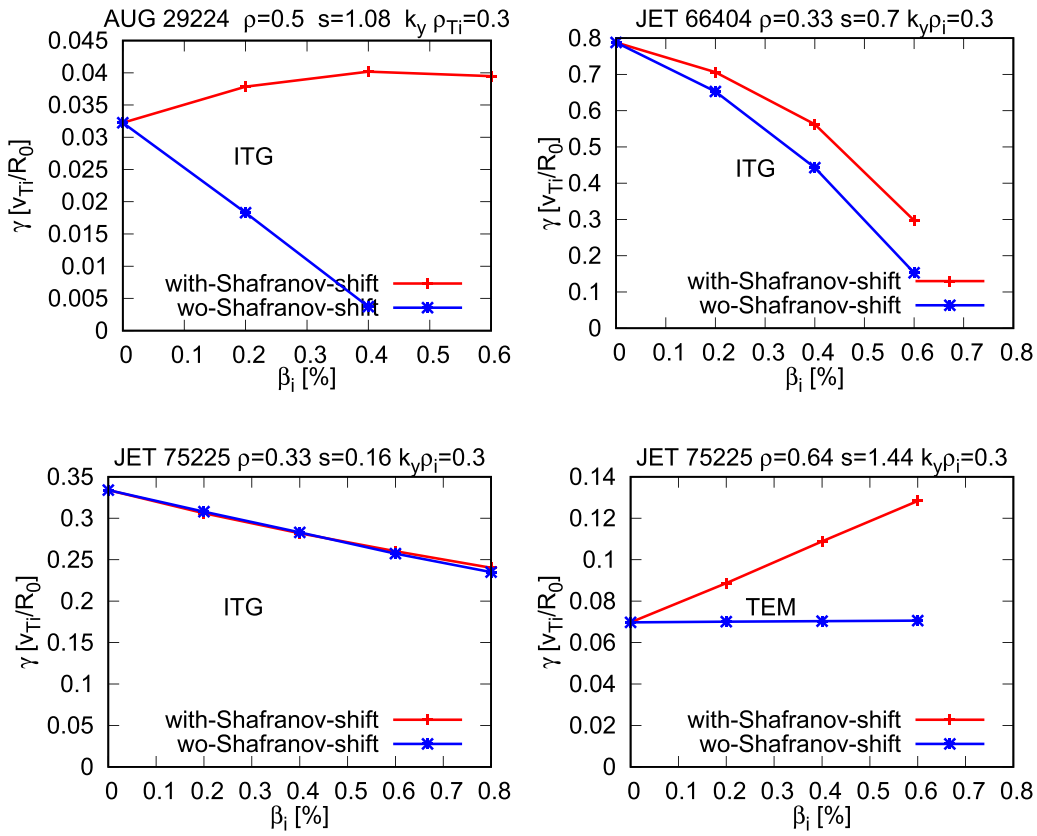

Figure 1. The linear growth rate as a function of β_i for AUG 29224 ($\rho = 0.5$, $s = 1.08$), JET 66404 ($\rho = 0.33$, $s = 0.7$), JET 75225 ($\rho = 0.33$, $s = 0.16$ and $\rho = 0.64$, $s = 1.44$) parameters with the Shafranov shift and without the Shafranov shift.

AUG shot No. 29224 ($s = 1.08$), moderate for the JET shot No. 66404 ($s = 0.7$), and negligible for the JET shot No. 75225 ($s = 0.16$ at $\rho = 0.33$). This implies that the enhancement of the growth rate by the Shafranov shift increases as the magnetic shear increases. For the JET shot No. 75225 parameters, the ITG mode is unstable at the core region ($\rho = 0.33$), while the TEM is unstable near the edge region ($\rho = 0.64$). The linear growth rate of the TEM is not influenced by magnetic fluctuations in wo-Shafranov-shift scan, and there is no electromagnetic stabilization with increasing β as shown by many gyrokinetic simulations [9, 10, 12, 37]. As a result of the Shafranov shift effect, the growth rate of TEM increases with β in the with-Shafranov-shift scan.

Here, we discuss the mechanism of a higher efficiently of the Shafranov shift for larger magnetic shear. That is attributed to the difference of mode structures along the magnetic field line shown in figure 2, where z is the coordinate along the field line. In most of the cases, the amplitude of electrostatic potential is large in the location $-\pi < z < \pi$ which is the outer-board of the torus called the bad curvature region. For the weak magnetic shear case JET shot No. 75225 ($s = 0.16$ at $\rho = 0.33$), by contrast, the mode is elongated up to $|z| \simeq 3\pi$. Since z is proportional to the poloidal angle θ, the effect of the Pfirsch-Schluter current $J_{PS} = \frac{2q}{B}\frac{dp}{dr}\cos\theta$ is averaged out when the mode structure is elongated. As a result, the Shafranov shift due to the Pfirsch-Schluter current does not affect instabilities for weak magnetic shear plasmas.

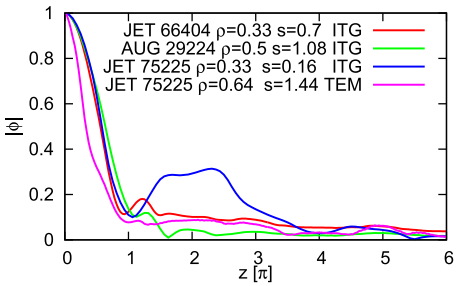

Figure 2. Profile of electrostatic potential fluctuation along the magnetic field line for JET 66404 ($\rho = 0.33$, $s = 0.7$), AUG 29224 ($\rho = 0.5$, $s = 1.08$), JET 75225 ($\rho = 0.33$, $s = 0.16$ and $\rho = 0.64$, $s = 1.44$) parameters.

In order to confirm the magnetic shear dependence of the Shafranov shift effect, we artificially increase or decrease the magnetic shear and calculate the linear growth rate as shown in figure 3. When we increase the magnetic shear from $s = 0.16$ to 0.7 for the JET shot No. 75225 at $\rho = 0.33$, the Shafranov shift effect clearly enhances the growth rate of the ITG mode. On the other hand, when we decrease the shear from $s = 1.44$ to 0.2 for the JET shot No. 75225 at $\rho = 0.64$, the enhancement of the growth rate of the TEM by the Shafranov shift becomes very small.

We conclude that the Shafranov shift effect reduces the electromagnetic stabilization of the ITG mode, and is small

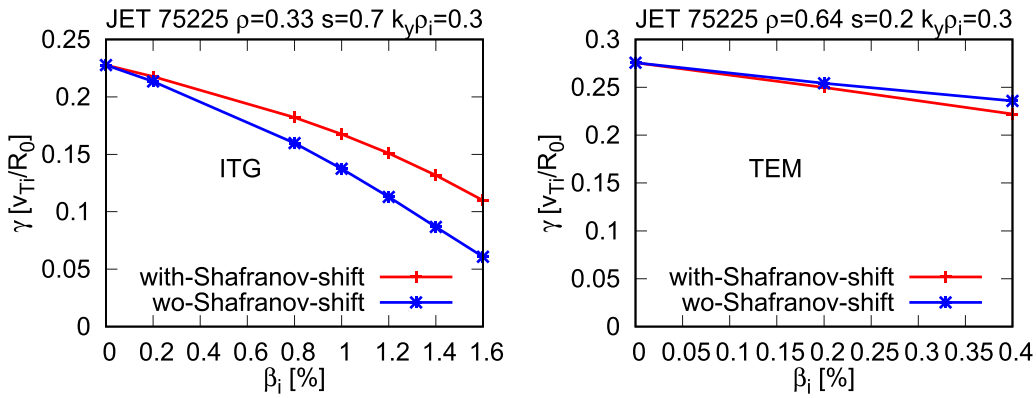

Figure 3. The linear growth rate as a function of β_i obtained by artificially increased/decreased magnetic shear for JET75225 at $\rho = 0.33$ ($s = 0.16$) and at $\rho = 0.64$ ($s = 1.44$).

for weak magnetic shear plasmas. The Shafranov shift also enhances the growth rate of the TEM. By using more precise numerical MHD equlibrium states, we also found that the electromagnetic stabilization is canceled out by the increase of the Shafranov shift, and thus the growth rate of the ITG mode does not decrease as β increases [23].

2.2. β dependence of turbulent transport evaluated from nonlinear simulations

Here, we present nonlinear simulation results on the β dependence of the turbulent energy and particle transport coefficients $\chi_s = Q_s L_{Ts}$ and $D_s = \Gamma_s L_{ns}$, where L_{Ts} and L_{ns} are the temperature and density gradient lengths, respectively, and s denotes particle species. The energy flux is $Q_s = \Theta_s + \frac{5}{2} T_s \Gamma_s$ [12, 48], where $\Theta_s = \Theta_{es,s} + \Theta_{em,s}$ and $\Gamma_s = \Gamma_{es,s} + \Gamma_{em,s}$. The turbulent thermal transport flux caused by the electrostatic and magnetic fluctuations, and the particle transport flux caused by the electrostatic and magnetic fluctuations are defined as

$$\Theta_{es,s} = \sum_{\mathbf{k}_\perp} \left\langle Re \left[\left(\frac{1}{2} \delta\hat{p}_{\parallel s\mathbf{k}_\perp} + \delta\hat{p}_{\perp s\mathbf{k}_\perp} - \frac{5}{2} T_s \delta\hat{n}_{s\mathbf{k}_\perp} \right) \left(\frac{-ik_y \phi_{\mathbf{k}_\perp}}{B} \right)^* \right] \right\rangle, \tag{1}$$

$$\Theta_{em,s} = \sum_{\mathbf{k}_\perp} \left\langle Re \left[\left(\frac{1}{2} \delta\hat{q}_{\parallel s\mathbf{k}_\perp} + \delta\hat{q}_{\perp s\mathbf{k}_\perp} \right) \left(\frac{ik_y A_{\parallel \mathbf{k}_\perp}}{B} \right)^* \right] \right\rangle, \tag{2}$$

$$\Gamma_{es,s} = \sum_{\mathbf{k}_\perp} \left\langle Re \left[\delta\hat{n}_{s\mathbf{k}_\perp} \left(\frac{-ik_y \phi_{\mathbf{k}_\perp}}{B} \right)^* \right] \right\rangle,$$

$$\Gamma_{em,s} = \sum_{\mathbf{k}_\perp} \left\langle Re \left[\delta\hat{u}_{s\mathbf{k}_\perp} \left(\frac{ik_y A_{\parallel \mathbf{k}_\perp}}{B} \right)^* \right] \right\rangle. \tag{3}$$

The flux surface average is represented by $\langle\rangle$. In these equations $\delta\hat{n}_{s\mathbf{k}_\perp} = \int \delta f_{s\mathbf{k}_\perp} J_{0s} d^3v$, $\delta\hat{u}_{s\mathbf{k}_\perp} = \int v_\parallel \delta f_{s\mathbf{k}_\perp} J_{0s} d^3v$, $\delta\hat{p}_{\parallel s\mathbf{k}_\perp} = \int m_s v_\parallel^2 \delta f_{s\mathbf{k}_\perp} J_{0s} d^3v$, $\delta\hat{p}_{\perp s\mathbf{k}_\perp} = \int \mu B \delta f_{s\mathbf{k}_\perp} J_{0s} d^3v$, $\delta\hat{q}_{\parallel s\mathbf{k}_\perp} = \int m_s v_\parallel^3 \delta f_{s\mathbf{k}_\perp} J_{0s} d^3v - 3T_s \delta\hat{u}_{s\mathbf{k}_\perp}$ and $\delta\hat{q}_{\perp s\mathbf{k}_\perp} = \int \mu B v_\parallel \delta f_{s\mathbf{k}_\perp} J_{0s} d^3v - T_s \delta\hat{u}_{s\mathbf{k}_\perp}$. Details are described in [12].

Figure 4 shows the β dependence of the ion and electron energy diffusivity coefficients χ_i and χ_e, and the ion and electron particle diffusivity coefficients D_i and D_e for JET No. 66404 ($s = 0.7$). The ion energy transport χ_i decreases with increasing β for wo-Shafranov-shift β scan, because the linear growth rate of the ITG mode decreases with β as shown in figure 1. On the other hand, χ_e increases with β. For with-Shafranov-shift scan, χ_i and χ_e are larger than those for wo-Shafranov-shift, and increase with β_i. Thus, the turbulent energy transport does not decrease with β_i because of the Shafranov shift effect. The ion and electron particle diffusion coefficients are the same $D_i = D_e$ because of the ambipolarity condition. The particle diffusion remains a similar level with increasing β for wo-Shafranov-shift scan, while the diffusion increases with β for the with-Shafranov-shift scan. Thus, both of the energy and particle transport coefficients increase with increasing β. A possible explanation on the increase of transport is the suppression of zonal flows. Since zonal flows are suppressed by stochastic magnetic field, the zonal flow level decreases as the amplitude of magnetic fluctuation increases with β as shown by [10], in fact, an intermittent enhancement of turbulent transport as a result of zonal flow suppression with increasing β is reported in [23]. We also observed the non-decrease of χ_i for the the AUG shot No. 29224 parameters in [22]. Figure 5 shows turbulent transport for the JET No. 75225 at $\rho = 0.33$ with artificially increased magnetic shear from $s = 0.16$ to 0.7 that leads to an enhanced linear growth rate by the Shafranov shift in figure 3. For the wo-Shafranov-shift scan, χ_i, χ_e and $D_i = D_e$ decrease with increasing β_i and are negligibly small at $\beta_i = 0.6\%$. For the with-Shafranov-shift scan, by contrast, all of χ_i, χ_e and $D_i = D_e$ do not decrease up to $\beta_i = 0.4\%$, and they decrease but are finite at $\beta_i = 0.6\%$. Thus, the Shafranov shift effect enhances the turbulent transport to be finite from negligibly small value. It is remarked that turbulent transport coefficients are very small at $\beta_i = 0.6\%$ in figure 5, which is the exceptional result showing very low turbulent transport from our nonlinear simulations. A possible explanation is that the artificially increased magnetic shear

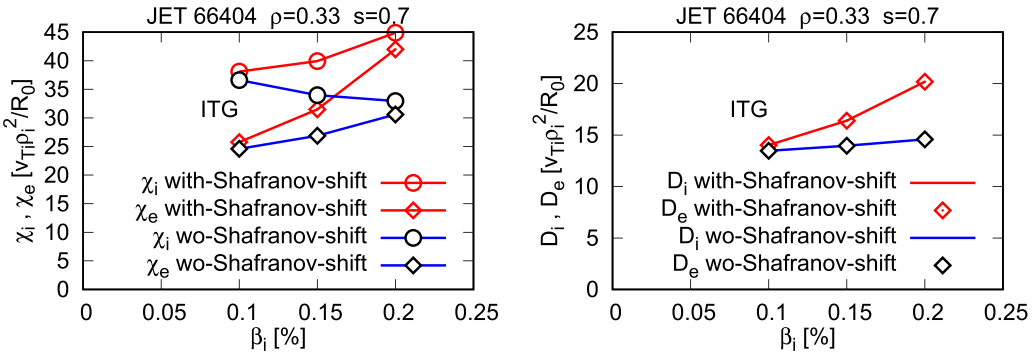

Figure 4. The β dependence of the ion and electron energy diffusivity coefficients χ_i and χ_e and the ion and electron particle diffusivity coefficients D_i and D_e, at $\rho = 0.33$ ($s = 0.7$) in JET No. 66404 for the magnetic field changed scan (with Shafranov shift) and the magnetic field fixed scan (without Shafranov shift).

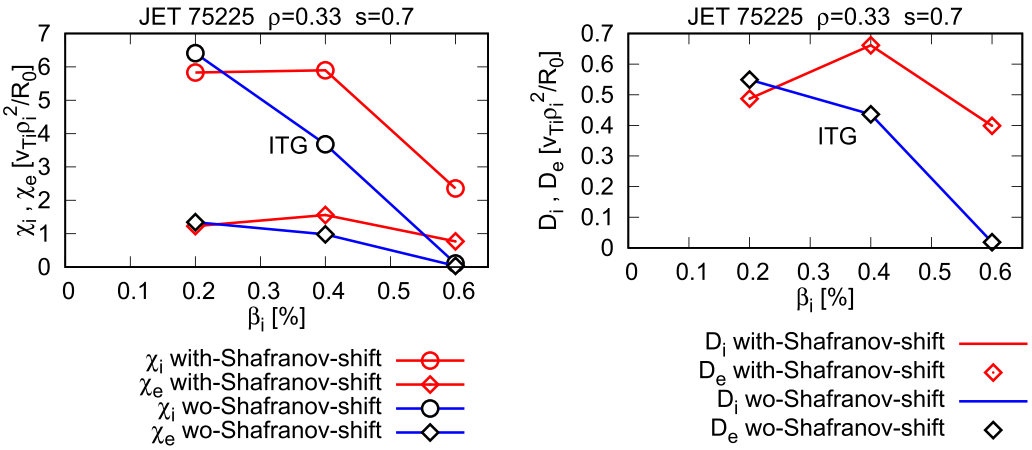

Figure 5. The β dependence of the ion and electron energy diffusivity coefficients χ_i and χ_e and the ion and electron particle diffusivity coefficients D_i and D_e by the ITG turbulence at $\rho = 0.33$ in JET No. 75225 with artificially increased magnetic shear from $s = 0.16$ to 0.7.

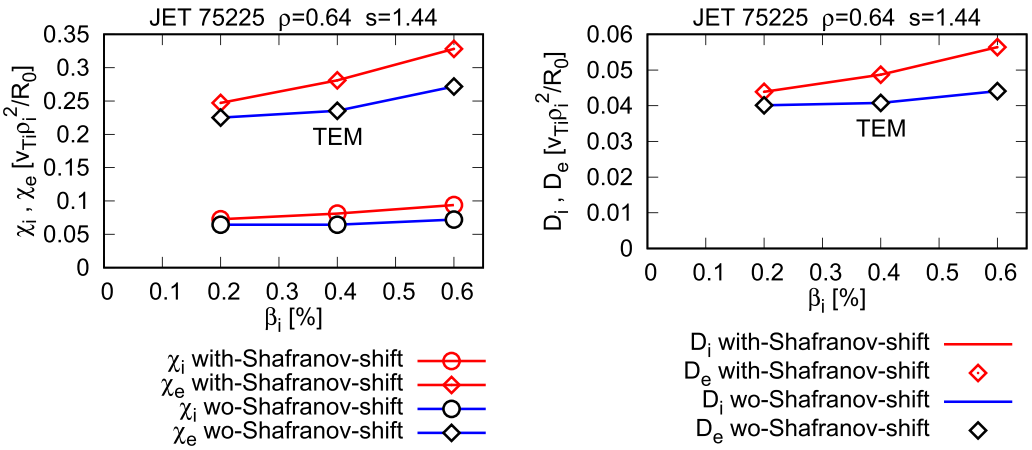

Figure 6. The β dependence of the ion and electron energy diffusivity χ_i and χ_e and the ion and electron particle diffusivity D_i and D_e by the TEM turbulence at $\rho = 0.64$ ($s = 1.44$) in JET No. 75225.

causes this exceptional result, in fact, we artificially increase the magnetic shear from $s = 0.16$ to 0.7 in figures 3 and 5.

We also found similar enhancement of TEM turbulent transport by the Shafranov shift effect. Figure 6 shows χ_i, χ_e, D_i and D_e due to the TEM turbulence at $\rho = 0.64$ in the JET shot No. 75225. The electron energy diffusivity χ_e is much higher than the ion diffusivity χ_i because of the TEM turbulence. For wo-Shafranov-shift scan, χ_i, χ_e, D_i, and D_e slightly increase with β, while they increase more rapidly with β for with-Shafranov-shift scan. Thus, the turbulent transport due to TEM increases with β, and the Shafranov shift effect enhances the turbulent transport.

In this section, we have presented that the electromagnetic stabilizing effect on the turbulent transport is canceled out by the Shafranov shift effect from local gyrokinetic simulations. We discuss the turbulent transport at higher β in the next section.

3. Exploring ITG turbulence at finite β regime by global simulations

We encounter a non-saturation of turbulence level at β above a critical value in evaluating the β dependence of turbulent transport by nonlinear local simulations. For instance, turbulent fluctuations continue to grow at $\beta_i > 0.2\%$ for JET 66404 case in figure 4. This non-saturation is common in local gyrokinetic simulations at finite β and known as the run-away/non-zonal transition [34, 35], and the critical onset β value is a fraction of the KBM onset β value [36]. Recently, steady turbulent states are obtained by global gyrokinetic simulations above the critical β value for the run-away/non-zonal transition [37–42]. In this section, we present global gyrokinetic simulation results for the CBC parameters by the electromagnetic GKNET code [49, 50] with the mass ratio m_i/m_e varying from 100 to 400 and ρ_* from 1/100 to 1/300. The choice of smaller m_i/m_e is to make the computations more affordable. We will present ITG turbulence at a β regime above $\beta_i = 0.65\%$, which is suffered from the non-zonal transition in local simulations [34, 35]. We have carried out two types of global simulations: one allows the background profile relaxation and the other is fixed-profile simulations. It is remarked that the influence of the Shafranov shift is not included in our global simulations.

3.1. Linear growth rate

First, we briefly describe results from linear analysis focusing on the mass ratio and ρ_* dependences of the linear growth rate because several sets of these parameters are used in our nonlinear simulations. Figure 7 shows the linear growth rate of the ITG mode as a function of $k_\theta \rho_{Ti}$ for CBC parameters as well as the growth rate from local analysis, where $k_\theta \rho_{Ti} = k_y \rho_{Ti}$ for local simulations, while $k_\theta \rho_{Ti} = \rho_* n q(r_s) r_s/a$ for global simulations, where $r_s = a/2$. Figure 7(a) shows that the growth rate for $m_i/m_e = 400$ is higher than that for the hydrogen mass ratio $m_i/m_e = 1836$ at $\beta_i = 0.2\%$ and $\rho_* = 1/100$. The linear growth rate of the ITG mode from global simulation is similar at low wavenumber and higher at high wavenumber than that from local simulation, although the linear growth rate of the ITG mode from global simulations is expected to be lower than that from local simulations [51]. The cause of this difference is discussed in appendix. It is remarked that, in the global GKENT code, the polarization term is expanded in powers of $k_\perp^2 \rho_{Ti}^2$ in the Poisson equation, and the Pade approximation is used in the gyro-average. These are approximated forms of the Bessel functions and are valid at low wavenumber. The approximations can cause a deviation from local simulation results at high wavenumber. When we improve the approximation in the gyro-average in the global GKNET, we have a lower growth rate at high wavenumber, which will be reported in our next paper. We will report a comparison of results from global GKNET with those from local GKV in a separate paper in detail. Figure 7(b) shows that the growth rate increases with decreasing ρ_* for $\beta_i = 0.2\%$ and $m_i/m_e = 400$, which is observed in global gyrokinetic simulations [52–54]. Figure 8 shows that the ITG modes are unstable at $\beta_i = 0.2\%$ and 1%, and that the electromagnetic stabilization is observed because of the absence of the Shafranov shift.

3.2. Saturation of ITG turbulence at finite β

The saturation of ITG turbulence at finite β in global simulations is not due to the profile relaxation but a strong zonal flow excitation. Here, the influence of relaxation is investigated by linear analysis using relaxed profiles in our nonlinear simulations. Figure 9 shows the linear growth rate of the ITG mode as a function of β for $m_i/m_e = 100$ and $\rho_* = 1/100$. The growth rate of the ITG mode for the profile after the saturation of the instability is similar to that for the initial profile, and thus the saturation of the ITG mode is not caused by the profile relaxation.

The saturation of the ITG mode at finite β is caused by a strong zonal flow excitation, which is in contrast to weak zonal flow production in local simulations at finite β. The strong zonal flows are produced at the side of peaked envelop of fluctuations in the radial direction as shown in figure 10. Figure 10 shows the nonlinear zonal flow excitation by the ITG turbulence, i.e. the nonlinear entropy transfer from the turbulence to zonal flows ($n = 0$ mode) $T_{n=0}$ [41] as well as the electrostatic potential ϕ and vector potential $A_\parallel$ of the most unstable mode $n = 38$. The fluctuations of ϕ and $A_\parallel$ peak at $r/a \simeq 0.45$, while the zonal flow excitation $T_{n=0}$ peaks at $r/a \simeq 0.38$ and 0.53. The minimum of the nonlinear excitation $T_{n=0}$ is located at $r/a \simeq 0.45$, i.e. at where ϕ and $A_\parallel$ peak. This implies that the nonlinear zonal flow excitation is strong not at the peak of the turbulence but at the sides of the peak. As a result, nonlinear excitation of zonal flows avoids the erosion due to magnetic fluctuations, resulting in strong zonal flow production. Next, we discuss the mechanism of the strong zonal flow excitation at the edge of turbulent fluctuation envelop. Three-wave coupling function

$$S_s(n;n',n'') = \nabla \cdot (h_{s,n} h_{s,n''} \langle \tilde{\mathbf{v}}_{\mathrm{E}\times\mathrm{B},n'} \rangle_s) + v_{Ts} v_\parallel \langle \tilde{\mathbf{b}}_{n'} \rangle_s \cdot \nabla (h_{s,n} h_{s,n''}) - S_s(n'';n',n) \tag{4}$$

in the entropy transfer

$$T_n = -\sum_s \sum_{n',n''} \mathrm{Re} \left\langle \int \frac{T_s}{2F_{0s}B} \{S_s(n;n',n'') + S_s(n;n'',n')\} d^3v \right\rangle \delta_{n,-n'-n''} \tag{5}$$

consists of three parts: the transfer from the turbulence (third term), the radial advection of the entropy (first term), and

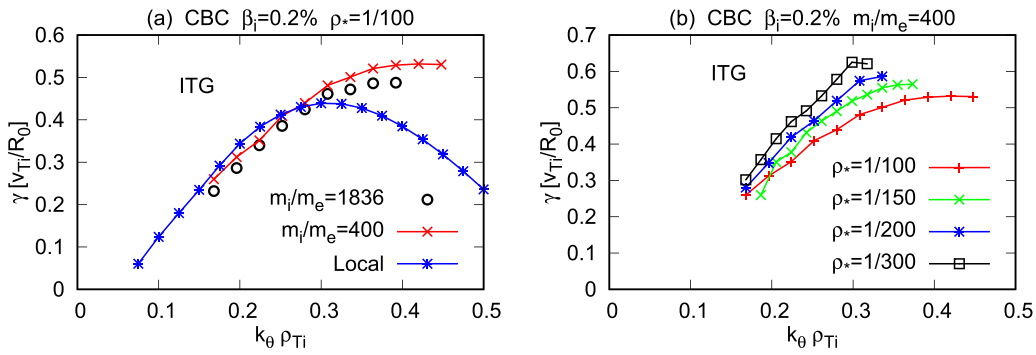

Figure 7. Linear growth rate from global simulations as a function of $k_\theta \rho_{Ti}$ for CBC parameters with (a) $\beta = 0.2\%$ and $\rho_* = 1/100$ including a local simulation result and (b) $\beta = 0.2\%$ and $m_i/m_e = 400$.

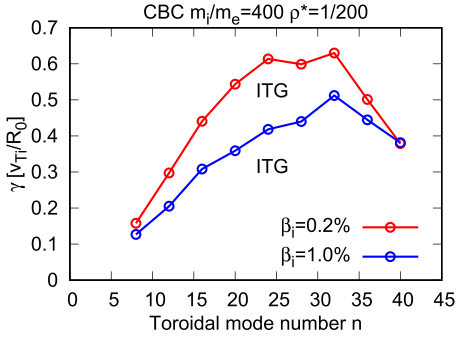

Figure 8. Linear growth rate of drift-wave instabilities for CBC parameters from global simulations.

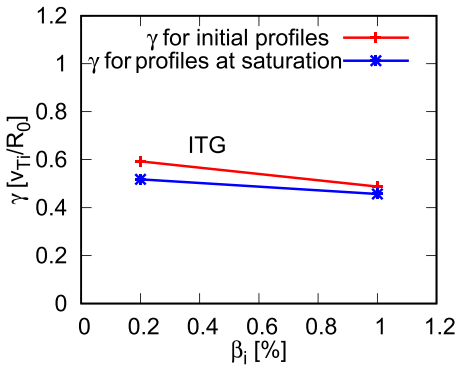

Figure 9. Linear growth rate of ITG mode using the initial profile and the relaxed profile after the saturation of turbulence in a nonlinear simulation for the CBC parameters with $m_i/m_e = 100$ and $\rho_* = 1/100$.

the radial magnetic diffusion (second term), where $\langle\rangle_s$ and $\langle\rangle$ denote the gyro-average and flux surface average, respectively. Details are described in [41]. These three terms are plotted in figure 10. The entropy transfer from the turbulence is positive and strong around the radius of $r/a = 0.45$. This transfer from the turbulence is canceled out by the radial advection term which is negative around the radius of $r/a = 0.45$, and is positive at the edge of the envelop of fluctuations, implying the entropy advection from the active to less active region. Hence, the nonlinear excitation of zonal flows is strong at the edge of the envelop of fluctuations. This entropy advection to less active region can be related to the turbulence spreading [55, 56]. It is remarked that the magnetic flutter term plays a minor role in the zonal flow production in this parameter regime.

The nonlinear excitation of zonal flows is strong at the edge of the envelop of turbulent fluctuations, even when we increase β to $\beta_i = 0.8\%$ and $1.\%$ as shown in figures 11 and 12. The width of the envelop is wider in figure 11 for $\rho_* = 1/200$ than that in figure 10 for $\rho_* = 1/300$, because the width of mode structure is proportional to $\sqrt{\rho}_*$. This is because the radial width of ballooning structure is proportional to $1/\sqrt{n}$ [57] and $n \propto m \propto a/\rho_{Ti} = 1/\rho_*$. When $\beta_i = 1\%$ the magnetic flutter term plays more important role in the three-wave coupling in figure 12(b), reducing the advection of entropy. As a result, the zonal flow excitation at the edge of the envelop is slightly suppressed at $\beta_i = 1.0\%$ in figure 12 compared to that at $\beta_i = 0.2\%$ in figure 10.

3.3. β dependence of turbulent transport evaluated from nonlinear simulations

We have obtained a steady state of turbulence in a finite-β regime, namely $\beta_i = 1.0\%$, such that the corresponding local simulations exhibit the non-saturation of turbulence, enabling us to evaluate the turbulent heat and particle fluxes in this β regime. Figure 13 shows the ion energy and particle fluxes as a function of β_i for $m_i/m_e = 100$ and $\rho_* = 1/100$ by the global simulations. It is remarked that the influence of the Shafranov shift is omitted in these simulations. The ion energy flux is due to the ITG turbulence and decreases with increasing β_i for both global and local simulations because of the electromagnetic stabilization in the absence of the Shafranov shift. The ion particle flux Γ_i decreases with β for $m_i/m_e = 100$, while increases with β for $m_i/m_e = 400$. The electron particle flux is very close to the ions $\Gamma_e \simeq \Gamma_i$ because of the intrinsic ambipolarity. The β dependence of the energy and particle fluxes from local and global simulations exhibit similar trend, however the transport levels from global simulations strongly depend on m_i/m_e and ρ_*. The higher turbulent transport level from the global simulation can be due to the higher linear growth rate shown in figure 7(a), which is discussed in appendix. We will report details of a comparison between global and local simulation results in a separate paper.

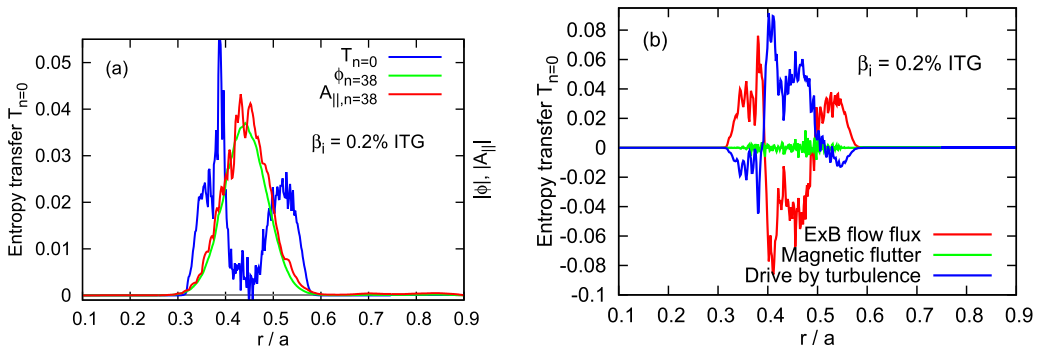

Figure 10. (*a*) Nonlinear entropy transfer to zonal modes $T_{n=0}(r)$ and the electrostatic and magnetic fluctuations, ϕ and $A_\|$, of the ITG turbulence at $\beta_i = 0.2\%$ for the CBC parameters with $m_i/m_e = 400$ and $\rho_* = 1/300$. (*b*) Each term of three-mode coupling to zonal modes $n = 0$, E×B convection, magnetic flutter, and transfer from high wavenumber drift-waves.

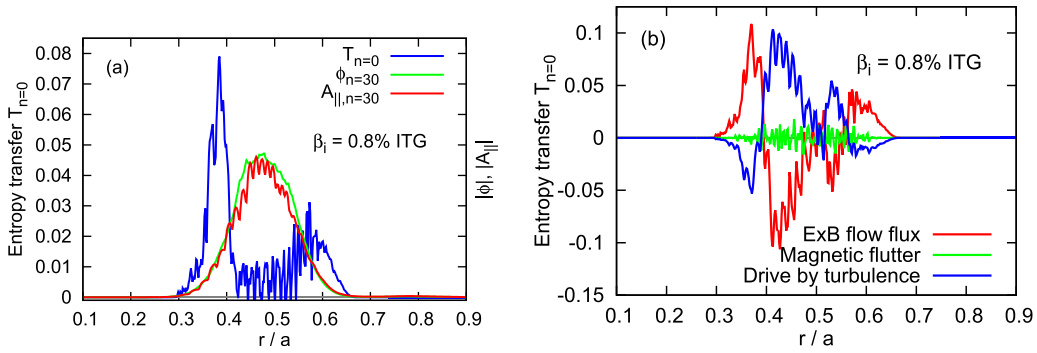

Figure 11. (*a*) Nonlinear entropy transfer to zonal modes $T_{n=0}(r)$ and ϕ and $A_\|$ of the ITG turbulence at $\beta_i = 0.8\%$ for the CBC parameters with $m_i/m_e = 400$ and $\rho_* = 1/200$. (*b*) Each term of three-mode coupling to zonal modes $n = 0$, E×B convection, magnetic flutter, and transfer from high wavenumber drift-waves.

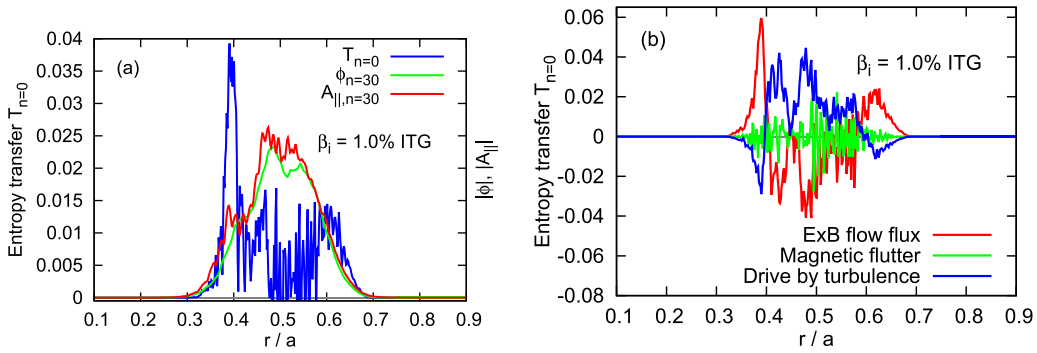

Figure 12. (*a*) Nonlinear entropy transfer to zonal modes $T_{n=0}(r)$ and ϕ and $A_\|$ of the ITG turbulence at $\beta_i = 1.0\%$ for the CBC parameters with $m_i/m_e = 400$ and $\rho_* = 1/200$. (*b*) Each term of three-mode coupling to zonal modes $n = 0$, E×B convection, magnetic flutter, and transfer from high wavenumber drift-waves.

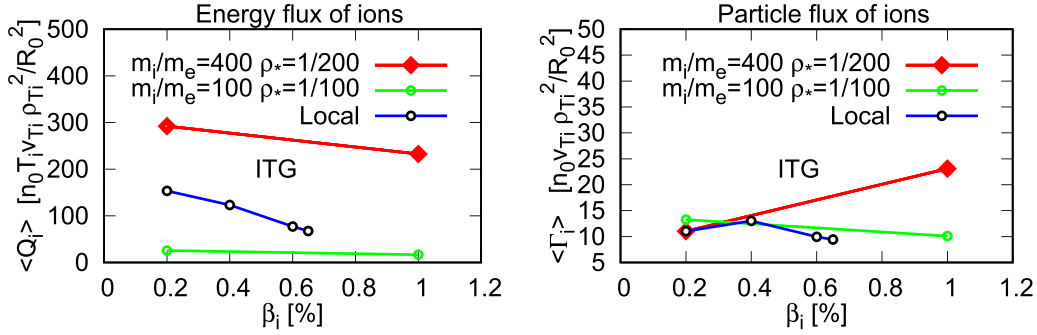

Figure 13. The β dependence of ion energy flux Q_i and ion particle flux Γ_i from fixed-profile simulations for CBC parameters.

4. Summary

Investigating the β dependence of ITG/TEM turbulence by nonlinear local simulations, we have found that the turbulent transport coefficients χ_i, χ_e, D_i and D_e do not decrease with increasing β, because the equilibrium magnetic field configuration is changed by the Pfirsch-Schluter current, i.e. the Shafranov shift. This is a consequence of the background magnetic field change enhancing the linear growth rate of the ITG mode as shown by the linear analysis. The growth rate is enhanced because the Shafranov shift suppresses the stabilizing effect of magnetic fluctuations through a decrease of the magnetic drift frequency ω_{Di}. That can be understood by expanding the fluid-like dispersion relation of electromagnetic ITG modes [6] for small β_i

$$\omega^2 = -\frac{T_e}{T_i}\omega_{Di}\omega_{*i}(1+\eta_i)\left(1-\beta_i\frac{\omega_{Di}\omega_{*i}}{2k_\perp^2\rho_{Ti}^2k_\parallel^2v_{Ti}^2}\right), \quad (6)$$

where ω_{*i} and β_i are the ion diamagnetic frequency and ion-beta [23], respectively, and $\omega_{Di}\omega_{*i} > 0$ at the bad curvature region. The magnetic field change also reduces the zonal-flow level by reducing the Maxwell stress which dominantly produces zonal flows in the steady turbulent state at finite β [22]. We also found that the electromagnetic stabilization is significant as the magnetic shear decreases because it leads to small $k_\parallel$ in equation (6), and thus the magnetic shear is one of the key parameters controlling the β dependence of ITG turbulence. In other words, the electromagnetic stabilization is prominent for weak magnetic shear. This suggests a better β dependence of the confinement for plasmas having a broad low-magnetic-shear region at the core such as the JET plasmas testing the hybrid scenario of ITER.

We may achieve a high-β regime by utilizing the hybrid scenario, then the next issue is to identify the turbulence that limits an achievable β, but we have a trouble in nonlinear gyrokinetic simulations in finite-β regime. Turbulence in finite β often exhibits non-saturation due to a lack of zonal flows above a critical β value equal to a fraction of the KBM stability limit in gyrokinetic simulations using radially localized flux tube geometry, in fact, we encounter the non-saturation at $\beta_i > 0.2\%$ for JET No. 66404 parameters in figure 4. The non-saturation is due to the suppression effect of magnetic fluctuations on zonal flows and is known as the run-away/non-zonal-transition [34–36]. On the other hand, strong zonal flows are excited even in high β regime in global gyrokinetic simulations (for instance [37]), because the radial location of the entropy transfer from turbulence to zonal flows avoids the active region of magnetic fluctuations [41]. The radial turbulent convection of the entropy excites the strong zonal-flow in global simulations, resulting in the steady state of the ITG turbulence at finite β. As a result, we are able to study the ITG turbulence at a higher β regime by global simulations than the corresponding local simulations and to evaluate turbulent transport. We will report details of comparison between turbulent transport from local and global simulations and discuss the influence of global effects such as the turbulence spreading.

Acknowledgments

One of the authors A I thanks to K Nakatani and H Masui for running the gyrokinetic simulation codes GKV and GKNET. This work was supported by the Japanese Ministry of Education, Culture, Sports, Science and Technology, Grant No. 17K06991. Simulations are performed on Plasma Simulator supercomputer at NIFS and JFRS-1 supercomputer at QST.

Appendix. Linear growth rates from global and local calculations

The linear growth rate of the ITG mode from global simulations is expected to be lower than that from local simulations [51]. However, the results in figure 7(*a*) show that the linear growth rate of the ITG mode from global simulations is similar at low wavenumber and higher at high wavenumber than that from local simulation. This is due to different forms of the gyrokinetic equation solved in the global GKNET and local GKV codes. In the global GKNET code, the gyrokinetic equation is written in the phase-space volume conserved form [45]. On the other hand, in the local GKV code, the gyrokinetic equation is written in term of the eikonal representation by utilizing the flute approximation $k_\perp \gg k_\parallel$ [12]. The influence of large aspect ratio approximation $a/R_0 \ll 1$ in these two representations of gyrokinetic equation may affect the linear growth rate of drift-wave instabilities. When we modify the gyrokinetic equation solved by GKNET into a similar form to the equation in GKV, then we have a lower linear growth rate of the ITG mode from GKNET as shown in figure 14, i.e. the growth rate from global simulations is lower than that from local simulations, consistent with the results in [51]. In addition, the growth rate from the global simulation is enhanced and is close to that from the local simulation as ρ_* decreases from 1/100 to 1/150. We will report a comparison between global and local simulation results in detail in a separate paper.

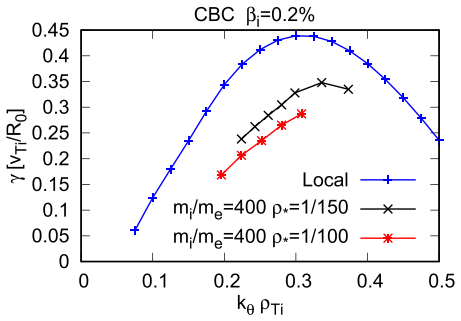

Figure 14. Linear growth rate as a function of $k_\theta \rho_{Ti}$ for CBC parameters with $\beta = 0.2\%$ and $m_i/m_e = 400$ from local and global calculations. It is noted that the gyrokinetic equation in global calculation is modified to into a similar form as that in local calculation in this figure.

ORCID iDs

A. Ishizawa https://orcid.org/0000-0002-5323-8448
S. Maeyama https://orcid.org/0000-0001-9338-0740

References

[1] Urano H., Takizuka T., Takenaga H., Oyama N., Miura Y. and Kamada Y. 2006 *Nucl. Fusion* **46** 781
[2] Vermare L. *et al* (The ASDEX Upgrade Team) 2007 *Nucl. Fusion* **47** 490
[3] Petty C.C. 2008 *Phys. Plasmas* **15** 080501
[4] McDonald D.C. *et al* (JET EFDA Contributors) 2008 *Plasma Phys. Control. Fusion* **50** 124013
[5] Challis C.D. *et al* 2015 *Nucl. Fusion* **55** 053031
[6] Kim J.Y., Horton W. and Dong J.Q. 1993 *Phys. Fluids* B **5** 4030
[7] Falchetto G.L., Vaclavik J. and Villard L. 2003 *Phys. Plasmas* **10** 1424
[8] Villard L. *et al* 2004 *Nucl. Fusion* **44** 172
[9] Candy J. 2005 *Phys. Plasmas* **12** 072307
[10] Pueschel M.J., Kammerer M. and Jenko F. 2008 *Phys. Plasmas* **15** 102310
[11] Pueschel M.J. and Jenko F. 2010 *Phys. Plasmas* **17** 062307
[12] Ishizawa A., Maeyama S., Watanabe T.-H., Sugama H. and Nakajima N. 2015 *J. Plasma Phys.* **81** 435810203
[13] Whelan G.G., Pueschel M.J. and Terry P.W. 2018 *Phys. Rev. Lett.* **120** 175002
[14] Citrin J., Jenko F., Mantica P., Told D., Bourdelle C., Garcia J., Haverkort J.W., Hogeweij G.M.D., Johnson T. and Pueschel M.J. 2013 *Phys. Rev. Lett.* **111** 155001
[15] Citrin J. *et al* (JET-EFDA Contributors) 2015 *Plasma Phys. Control Fusion* **57** 014032
[16] Doerk H., Dunne M., Jenko F., Ryter F., Schneider P.A. and Wolfrum E. 2015 *Phys. Plasmas* **22** 042503
[17] Garcia J., Challis C., Citrin J., Doerk H., Giruzzi G., Görler T., Jenko F. and Maget P. 2015 *Nucl. Fusion* **55** 053007
[18] Doerk H., Challis C., Citrin J., Garcia J., Görler T. and Jenko F. 2016 *Plasma Phys. Control. Fusion* **58** 115005
[19] Garcia J. (JET Contributors) 2022 *Plasma Phys. Control. Fusion* **64** 104002
[20] Mantica P. *et al* 2009 *Phys. Rev. Lett.* **102** 175002
[21] Mantica P. *et al* 2011 *Phys. Rev. Lett.* **107** 135004
[22] Ishizawa A., Urano D., Nakamura Y., Maeyama S. and Watanabe T.-H. 2019 *Phys. Rev. Lett.* **123** 025003
[23] Niiro M., Ishizawa A., Nakamura Y., Maeyama S. and Watanabe T.-H. 2023 *Plasma Phys. Control. Fusion* **65** 065004
[24] Connor J.W., Hastie R.J. and Taylor J.B. 1978 *Phys. Rev. Lett.* **40** 396
[25] Hirose A., Zhang L. and Elia M. 1994 *Phys. Rev. Lett.* **72** 3993
[26] Lapillonne X., Brunner S., Dannert T., Jolliet S., Marinoni A., Villard L., Gorler T., Jenko F. and Merz F. 2009 *Phys. Plasmas* **16** 032308
[27] Staebler G.M. 2018 *Nucl. Fusion* **58** 115001
[28] Miller R.L., Chu M.S., Greene J.M., Lin-Liu Y.R. and Waltz R.E. 1998 *Phys. Plasmas* **5** 973
[29] Stacey W.M. 2008 *Phys. Plasmas* **15** 122505
[30] Mulholland P., Aleynikova K., Faber B.J., Pueschel M.J., Proll J.H.E., Hegna C.C., Terry P.W. and Nuhrenberg C. 2023 *Phys. Rev. Lett.* **131** 185101
[31] Hatch D.R., Pueschel M.J., Jenko F., Nevins W.M., Terry P.W. and Doerk H. 2012 *Phys. Rev. Lett.* **108** 235002
[32] Terry P.W., Pueschel M.J., Carmody D. and Nevins W.M. 2013 *Phys. Plasmas* **20** 112502
[33] Williams Z.R., Pueschel M.J., Terry P.W. and Hauff T. 2017 *Phys. Plasmas* **24** 122309
[34] Waltz R.E. 2010 *Phys. Plasmas* **17** 072501
[35] Pueschel M.J., Terry P.W., Jenko F., Hatch D.R., Nevins W.M., Gorler T. and Told D. 2013 *Phys. Rev. Lett.* **110** 155005
[36] Pueschel M.J., Terry P.W. and Hatch D.R. 2014 *Phys. Plasmas* **21** 055901
[37] Ishizawa A., Imadera K., Nakamura Y. and Kishimoto Y. 2019 *Phys. Plasmas* **26** 082301
[38] Dong G., Bao J., Bhattacharjee A. and Lin Z. 2019 *Phys. Plasmas* **26** 010701
[39] Mishchenko A. *et al* 2021 *Plasma Phys. Control. Fusion* **63** 084007
[40] Mishchenko A. *et al* 2022 *Plasma Phys. Control. Fusion* **64** 104009
[41] Masui H., Ishizawa A., Imadera K., Kishimoto Y. and Nakamura Y. 2022 *Nucl. Fusion* **62** 074001
[42] Chen Y.C., Qin Y.Q., Sun G.Y., Dong G., Xiao Y. and Lin Z. 2023 *Phys. Plasmas* **30** 022302
[43] Ishida Y., Ishizawa A., Imadera K., Kishimoto Y. and Nakamura Y. 2020 *Phys. Plasmas* **27** 092302
[44] Kishimoto Y., Qin Z., Zhao R., Liu J., Imadera K., Wang W., Li J.Q., Kim J.Y. and Ishizawa A. 2023 Origin of profile constraint in toroidal plasmas with different magnetic structures leading to transport barrier *2023 IAEA Fusion Energy Conf. (London)* p IAEA-CN-316-1812
[45] Imadera K. and Kishimoto Y. 2023 *Plasma Phys. Control. Fusion* **65** 024003
[46] Watanabe T.-H. and Sugama H. 2006 *Nucl. Fusion* **46** 24
[47] Beer M.A., Cowley S.C. and Hammett G.W. 1995 *Phys. Plasmas* **2** 2687
[48] Li J. *et al* 2021 *Nucl. Fusion* **61** 126008
[49] Imadera K., Kishimoto Y., Obrejan K., Kobiki T. and Li J.Q. 2014 Global profile relaxation coupled with ExB staircase in toroidal flux-driven ITG turbulence *25th IAEA Int. Conf. on Fusion Energy (St. Petersburg)* p TH/P5-8
[50] Ishizawa A., Imadera K., Nakamura Y. and Kishimoto Y. 2021 *Nucl. Fusion* **61** 114002
[51] Gorler T., Tronko N., Hornsby W.A., Bottino A., Kleiber R., Norscini C., Grandgirard V., Jenko F. and Sonnendrucker E. 2016 *Phys. Plasmas* **23** 072503

[52] Gorler T., Lapillonne X., Brunner S., Dannert T., Jenko F., Merz F. and Told D. 2011 *J. Comput. Phys.* **230** 7053–71
[53] McMillan B.F., Lapillonne X., Brunner S., Villard L., Jolliet S., Bottino A., Gorler T. and Jenko F. 2010 *Phys. Rev. Lett.* **105** 155001
[54] Villard L. *et al* 2010 *Plasma Phys. Control. Fusion* **52** 124038
[55] Hahm T.S. and Diamond P.H. 2018 *J. Korean Phys. Soc.* **73** 747
[56] Gurcan O. D., Diamond P.H. and Hahm T.S. 2006 *Phys. Rev. Lett.* **97** 024502
[57] Connor J.W., Hastie R.J. and Taylor J.B. 1979 *Proc. R. Soc.* A **365** 1–17